applied sciences

MDPI

Article

Characteristics of the Temperature and Humidity Variations of Burial-Type Stone Relics and a Fitting Model

Ping Liu [1,*], Wentao Shi [1,*], Bo Sun [1,2,3], Qian Wang [1], Xiaokun Xie [1] and Changqing Li [3]

[1] College of Civil Engineering and Mechanics, Lanzhou University, Lanzhou 730000, China; xbysunbo@163.com (B.S.); 220220936391@lzu.edu.cn (Q.W.); xxk565807908@163.com (X.X.)
[2] Heritage Protection Science and Innovation Center, Northwest Research Institute Co. Ltd. of China Railway Engineering Corporation C.R.E.C, Lanzhou 730000, China
[3] School of Civil Engineering, Lanzhou University of Technology, Lanzhou 730050, China; lichangqing333@163.com
* Correspondence: liuping@lzu.edu.cn (P.L.); shiwt2023@lzu.edu.cn (W.S.)

Abstract: Burial stone relics remain in a humid, semi-enclosed environment for long periods, and temperature and humidity variations can cause deterioration acceleration. Yang Can's tomb was selected as the research object, and field monitoring and simulations were performed to investigate the characteristics of temperature and humidity variations, after which the simulation results were evaluated. The monitoring results showed that solar radiation, rainfall, wind speed, and depth of entry are important factors affecting the variation in the temperature and humidity of burial stone relics. The temperature outside the chamber is greatly affected by seasonal variations, while the humidity inside the chamber is influenced by seasonal variations, so appropriate measures should be implemented inside and outside the chamber during different seasons to alleviate deterioration. On the basis of the above analysis, a temperature and humidity model for the interior chamber of burial stone relics was established in COMSOL software 5.6, combined with a porous medium heat transfer model and computational fluid dynamics (CFD) model. The temperature and humidity inside the chamber can be calculated by the temperature and humidity outside the chamber. This study provides data support for hydrothermal, condensation and other related studies of burial stone relics.

Keywords: burial stone relics; temperature and humidity variations; seasonal patterns; COMSOL simulation; fitting model

check for updates

Citation: Liu, P.; Shi, W.; Sun, B.; Wang, Q.; Xie, X.; Li, C. Characteristics of the Temperature and Humidity Variations of Burial-Type Stone Relics and a Fitting Model. *Appl. Sci.* **2024**, *14*, 2157. https://doi.org/10.3390/app14052157

Academic Editor: Asterios Bakolas

Received: 1 February 2024
Revised: 23 February 2024
Accepted: 29 February 2024
Published: 5 March 2024

Copyright: © 2024 by the authors. Licensee MDPI, Basel, Switzerland. This article is an open access article distributed under the terms and conditions of the Creative Commons Attribution (CC BY) license (https://creativecommons.org/licenses/by/4.0/).

1. Introduction

Burial structures house the remains of the dead. In terms of the spatial relationship, a burial structure comprises two major systems, i.e., above- and below-ground systems. The above-ground system includes facilities such as burial mounds, mausoleums (cemeteries), mausoleum buildings, and Shinto stone carvings, while the below-ground system includes tomb shapes, tomb room decorations, coffins, burial goods and various burial objects [1]. Considering ancient traditions, the tomb is a place for long-term rest, so much attention was given to tomb decoration and durability aspects, and these needs could be satisfied by rock and stone carvings. Most tombs excavated and completed in China comprise natural rock, used for the construction of above- and below-ground systems. Therefore, the conservation of burial stone relics is an important part of heritage conservation. Southwest China exhibits a humid subtropical monsoon climate, with high temperatures, rainy summers, and mild winters with little rain. Burial stone relics remain in a semi-enclosed, humid environment for long periods, and notable variations in the temperature and humidity could cause deterioration acceleration. Consequently, there is an urgent need for conservation research on the characteristics of temperature and humidity changes of burial stone relics.

At present, research on the temperature and humidity of stone relics mostly entails the adoption of field measurement methods. On-site field measurements indicate that although

the acquisition of relic information is time consuming and costly, researchers must often obtain multiple consecutive data time series for use as a control. Therefore, it is necessary to explore and design a fast, nondestructive and low-cost temperature and humidity measurement method for stone artifacts, which can provide valuable references for the conservation and restoration of cultural relics. In recent years, the rapid development of computer simulation technology has provided new ideas to solve this problem. Among them, nonstationary hygrothermal coupling simulation technology and computational fluid dynamics (CFD) simulation technology have been widely used to obtain the change trends of the temperature, water content and other parameters of cultural relics. Various simulation techniques can be coupled to provide a scientific basis for heritage conservation while greatly reducing measurement costs.

Matsukura et al. aimed to improve the adaptability of the heat, air, and moisture (HAM) model to different environments, using the temperature (T) and moisture chemical potential (μ) as driving potential factors to establish a coupled μHAM model of the building body, which is more suitable for the simulation of heat–humidity coupling in different environments, yielding an enhanced calculation accuracy [2]. Belleghem et al. [3] presented a newly developed heat and mass transfer model implemented in 3D finite volume solver Fluent, allowing for simultaneous modeling of the convective conditions around porous materials and heat and moisture transfer in porous materials controlled by diffusion. In contrast to most HAM models, which are usually limited to constant convective transfer coefficients, it is now possible to better predict these convective boundary conditions [3]. Gu, Luo and Song proposed the idea that large open spaces in archeological museums could lead to relic deterioration, demonstrating the necessity of introducing localized environmental control of pits. Moreover, they conducted CFD simulations to propose optimal preservation criteria for relics, seeking to ensure a balance between visitor comfort and relic protection [4–6]. An used CHAMPS-BES model to simulate transient heat and moisture coupling considering relic heat, moisture and other data of cliff statues in the Guangfo Cliff Grottoes, Sichuan, and the simulation results indicated a high accuracy, thus providing theoretical support for the protection of stone relics [7]. Araoka et al. [8] investigated the damage to the Nanjing city wall and proposed a model for rainwater infiltration into the wall. The simulation results showed that rainwater infiltration gradually affects the water content in bricks and mortar inside the wall [8]. Chang et al. proposed a system using evaporative cooling and ultrasonic humidification devices to control the local environment in relic conservation areas and to provide supersaturated relative humidity conditions for inhibiting soil cracking [9]. Agnieszka Sadłowska-Sałęga and JC Radon monitored the indoor conditions and external climate of an 18th century wooden church in Wiśniowa (Poland). The results of year-round simulations were compared with those of an experimental study resulting from model calibration, which, in addition to the goodness of fit, provided sufficient flexibility [10]. Luo et al. conducted localized environmental management of museum burial pits at the site of the Mausoleum of Qin Shi Huang [11]. Francesca Frasca et al. [12] outlined a multistep approach to investigate the ability of BES tool coupled with the HAM model (BES + HAM) as a diagnostic and preservation technique in complex environments. The 17th century Church of Santa Rosalia (Italy) was used as a historical monument within an authentic context, and it was demonstrated that the BES + HAM tool could be used to identify potential moisture-induced conservation risks [12]. Bi et al. [13] analyzed hygrothermal transfer in the cave wall of Mogao Cave experimentally and numerically. A one-dimensional model of moisture–heat coupling was established to simulate the moisture and heat behavior patterns of Mogao Cave walls with the temperature and water vapor pressure as driving potentials. The model provides theoretical support and a scientific methodology for the conservation of cave sites, while mural paintings should still be quantitatively analyzed [13]. Xiong et al. [14] investigated the changes in heat and humidity conditions during the burial period of the Mausoleum of Zhang Anshi from tomb sealing to excavation by means of on-site tests and CFD modeling. Moreover, it was noted that drastic changes in the heat and

humidity environmental conditions could trigger deterioration of historical relics. The local annual average temperature should be considered in the protection of underground relics excavated from the thermostatic layer of soil. This study paved the way for describing the environment of ancient burial chambers, museum design, energy conservation, and support for cultural heritage preservation and preventive conservation [14]. Tarek A. Mouneer et al. [15] adopted three approaches, namely: (i) experimental work, (ii) CFD simulation, and (iii) cooling load analysis. Temperature distributions were measured for establishing a reduced model of a mosque and a church, and CFD modeling (with the MSJ-CFD model) was performed to study the flow fields associated with two configurations under three distinct scenarios [15]. Xu et al. [16] investigated the potential effect of coupled moisture–heat migration on the heat transfer characteristics of buried pipes through a series of modeling tests. A three-dimensional model considering the variation in the soil thermal conductivity with temperature was established and validated. The model was utilized to further evaluate the effects of the heat storage temperature and initial soil moisture content on the heat transfer characteristics of buried pipes [16]. Liu et al. [17] proposed an energy-balanced routing protocol that could minimize the energy consumption of the network. An improved artificial intelligence population optimization algorithm combining particle swarm and ant colony optimization techniques was used to construct an environmental monitoring system for relic protection [17]. Cao and Li simulated and predicted the spatial and temporal patterns in 2030 and 2060 using the cellular automata (CA) model and landscape index and assessed the achievement of the carbon peaking and carbon neutrality targets [18]. Xia et al. [19] investigated the distributions of salt crystallization and microbial growth in two tombs through long-term (annual) environmental monitoring and short-term (monthly) surveys. It was concluded that microclimate control is crucial for inhibiting mural deterioration and should be emphasized in the future [19]. Liu et al. [20] developed a mathematical model of indoor heat and moisture transfer based on an ancient wooden palace building in Beijing. The model was validated against measured and simulated data through fitting. The results showed that both the measured and simulated data occur within the error range, verifying the accuracy of the developed model [20]. The simulation results of the indoor humidity matched the measured humidity data. Therefore, the simulation results are consistent with the actual conditions.

Burial relics are housed in unique environments, with concrete waterproof structures built around the perimeter of the burial chamber and covered with soil, producing highly complex heat and moisture distributions inside the chamber. Building envelope heat and moisture transfer models and CFD airflow models are commonly used in existing research. However, building envelope heat and moisture transfer models do not consider the effects of air exchange inside and outside the building on heat and moisture transfer, while CFD airflow models do not consider heat and moisture migration inside the wall. In this paper, these two types of models are combined for the first time, and a coupled heat and humidity transfer–CFD airflow model is applied to tomb-type stone relics. To monitor the meteorological parameters inside and outside Yang Can's tomb, the characteristics of the spatial and temporal distributions of the meteorological parameters of stone relics of the tomb category, the change pattern and the influencing factors were first obtained. The heat and humidity transfer–CFD airflow model was then employed in simulations. Through the comparison of the measurement and simulation results, it could be concluded that the model provides greater applicability to the simulation of heat and humidity transfer in tomb-like stone artifacts under the action of airflow. The proposed heat and humidity transfer–CFD airflow model is a new, highly accurate and economical method for predicting the temperature and humidity of stone artifacts based on COMSOL software 5.6. It is very important to investigate the variation patterns of the temperature and humidity of tomb-like stone artifacts and deepen the research on the water vapor condensation mechanism.

2. Field Monitoring

2.1. Monitoring Object

The field monitoring object in this study is Yang Can's tomb, located in the southern part of Honghuagang District, Zunyi city, Guizhou Province, 10 km south of Huangfenzui. The geographic location is shown in Figure 1. In 1982, the State Council announced the second batch of national key cultural relic protection units. It is the largest stone tomb of the Song Dynasty in Guizhou, Southwest China, and one of four major Tusi, or Yang family cultural relics, representing one of the most important relics. Yang Can's tomb, with its outstanding architecture and stone carvings, is referred to as a treasure of the art of ancient stone carvings in Southwest China. It is a rarity among Chinese ancient tombs, with notable historical, cultural and artistic value. Yang Can's tomb was constructed during the Chun You reign of Emperor Li Zong of the Song Dynasty (1241–1252), and it was mainly constructed of rock, making it a typical stone relic of the tomb category [21].

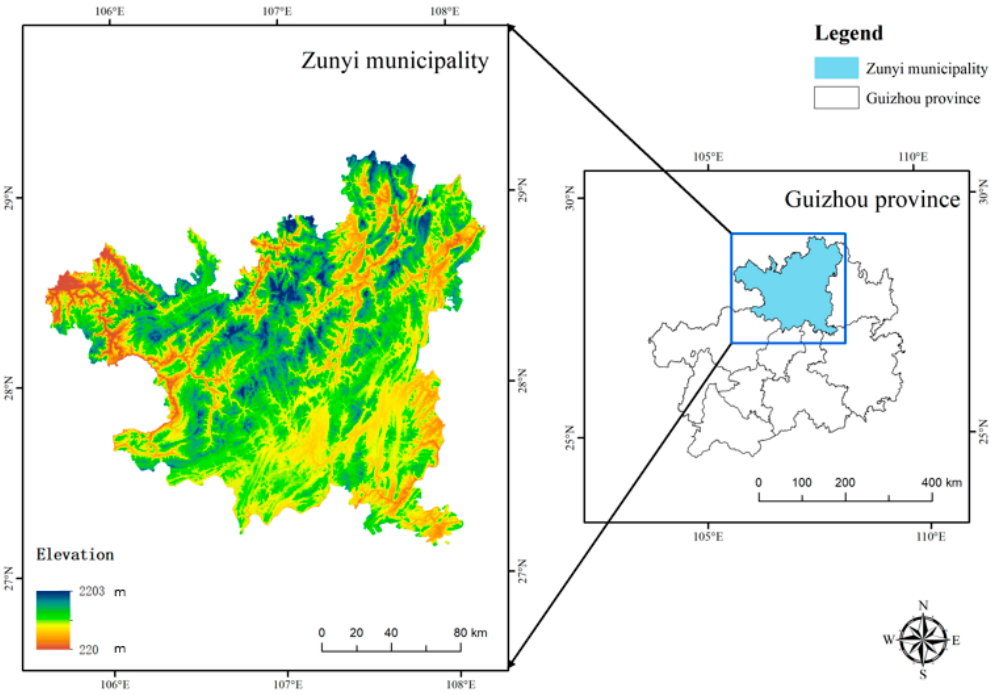

Figure 1. Map of the location of Yang Can's tomb.

Considering the irreversibility of the destruction of cultural relics as well as the specificity of cultural relic protection, a small number of in situ sandstone samples were obtained from Yang Can's tomb, and the thermal and humidity parameters of the sampled sandstone were systematically determined indoors (refer to Table 1). The density was measured using a hydrostatic balance (model: JA 5003) in combination with the wax seal method. Isothermal moisture absorption and release curves were obtained using desiccators containing silica gel desiccant (five humidity levels). The water vapor permeability coefficient of the sandstone specimens was determined using the desiccant method. In accordance with international standard ISO 15148:2002(E) [22], the specimens were immersed on one side to measure the liquid water transfer coefficient. The thermal conductivity and thermal diffusion coefficient of the specimens were obtained by a thermal constant analyzer (model: Hot disk TPS2500s). Parametric support was provided for the subsequent computer simulations.

2.2. Monitoring Methods

By reviewing previous investigation data and combining them with the actual conditions of the Yang Can tomb site, a continuous and fixed monitoring method was adopted to conduct long-term monitoring of the environmental meteorological parameters inside

and outside the burial chamber, such as the air temperature and humidity, solar radiation, rainfall, and wind speed.

Table 1. Thermo-hygroscopic parameters of the sandstone from Yang Can's tomb.

Density (g/cm^3)	Isothermal Hygroscopic Curve	Water Vapor Permeability Coefficient ($g/(Pa\ s\ m^2)$)	Liquid Water Diffusion Coefficient (m/s^2)	Thermal Conductivity (W/(m K))	Specific Heat (J/(kg K))
2.42	$u = e^{-4.81+0.053\varphi}$	2.33×10^{-7}	4.49×10^{-6}	2.54	863

2.2.1. Monitoring of the Meteorological Parameters Outside the Burial Chamber

Yang Can's tomb exhibits geomorphological features and is subjected to local wind conditions. A meteorological monitoring station was deployed outside the tomb in the open area at the top of the tomb. Notably, the wind direction sensor faced east, the detection frequency was set to 30 min, and the specific deployment location is shown in Figure 2a.

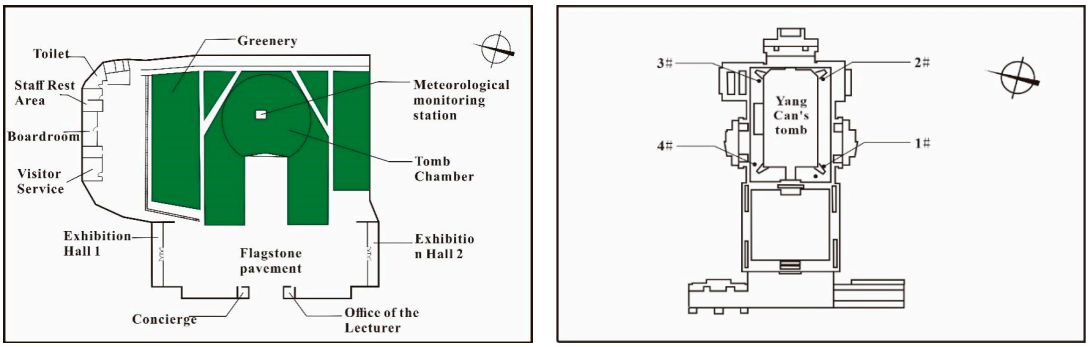

(**a**) (**b**)

Figure 2. Plan of Yang Can's tomb and location of the meteorological stations outside and inside the chamber: (**a**) outside the chamber; (**b**) inside the chamber.

2.2.2. Burial Chamber Environmental Data Monitoring

As the female chamber of Yang Can's tomb has been preserved by the local museum, the monitoring process mainly focused on the male chamber, and the chamber plan is shown in Figure 2b. Since tourists visit the tomb regularly, the sensors were arranged in the tomb while fully ensuring their concealment. Therefore, the temperature and humidity recording devices and sensors were installed near the tomb and supported by a bracket to ensure the validity of the data recording process while considering aesthetics. Temperature and humidity data of the chamber were collected at 30-min intervals. Notably, points "#1" and "#4" were arranged at smaller depths, while points "#2" and "#3" were arranged at larger depths. Points "#1" and "#2" served as monitoring points at different depths on the same side, points "#1" and "#4" served as monitoring points at the same depth on different sides, and points "#1" and "#3" served as monitoring points at different depths on different sides.

2.3. Monitoring Instruments

The meteorological parameters outside the burial chamber were monitored using a meteorological monitoring station.

Tomb indoor environmental data were recorded using a temperature and humidity logger (model: TH10R), with a temperature measurement range of −40 °C to 80 °C, a humidity measurement range of 0–100% relative humidity (RH), a temperature measurement accuracy of ±0.5 °C and a humidity measurement accuracy of ±5% RH.

3. Temperature and Humidity Characteristics of Yang Can's Tomb and Their Variation Patterns

3.1. Annual Variation Patterns of the Temperature and Humidity in the Burial Chamber

3.1.1. Temperature Variations

As shown in Figure 3a, the temperatures inside and outside the chamber of Yang Can's tomb varied throughout the year. No data were collected from April to early May due to equipment upgrades. The temperature outside the chamber was highly responsive to seasonal variations, and the season variation was high. The temperature outside the chamber reached an annual maximum value of 37.8 °C in August and then began to decrease, reaching an annual minimum value of −1.4 °C in January, thus yielding a yearly temperature difference of 39.2 °C. The temperature inside the chamber was less responsive to seasonal variations, and the seasonal variation magnitude was small. The temperature inside the chamber gradually increased from February to August, reaching a maximum value of 26.5 °C in August, after which it began to decrease, reaching an annual minimum value of 4.8 °C in January, thus yielding a temperature difference of 21.7 °C throughout the year. In summer, gas exchange inside and outside the chamber was not intense, and heat transfer was reduced. Therefore, the temperature variations inside the chamber remained more stable in the summer months.

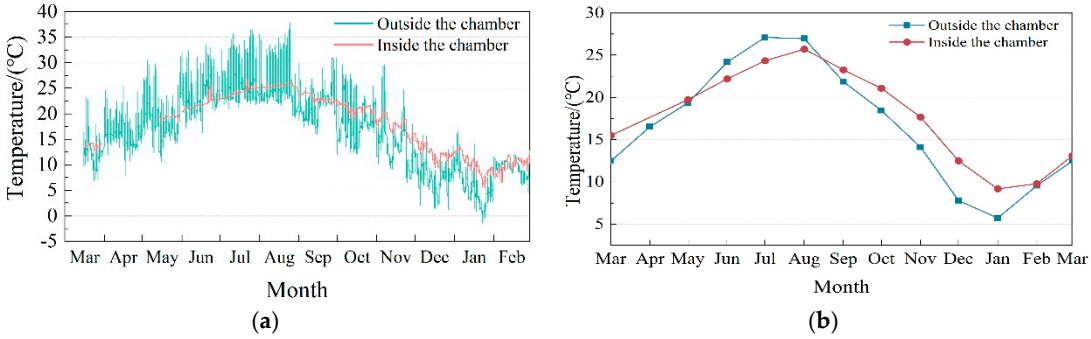

Figure 3. Temperature variations inside and outside the chamber: (**a**) variations throughout the year; (**b**) average monthly variations.

The average monthly temperatures inside and outside the chamber (Figure 3b) were analyzed. From the perspective of the monthly average temperature, the temperatures both inside and outside the tomb reached maximum values in summer and minimum values in winter, with obvious seasonal characteristics. However, due to the insulating effect of the subterranean system of the chamber, the temperature inside the chamber was less sensitive to seasonal variations, and the temperature peaks inside the chamber exhibited a certain lag. The minimum monthly mean temperature inside the chamber was 3.45 °C higher than that outside the chamber, indicating that the underground system of the chamber was well insulated. In summer, the temperature outside the chamber was higher than that inside the chamber, and heat was transferred from outside to inside. In winter, the temperature outside the chamber was lower than that inside the chamber, and heat was transferred from inside to outside.

3.1.2. Variations in the Relative Humidity

Figure 4a shows a comparison of the relative air humidity levels inside and outside Yang Can's tomb throughout the year. The figure reveals that the relative humidity outside the chamber varied more widely and was less responsive to seasonal variations than that inside the chamber, and the relative humidity remained high throughout the year. Affected by rainfall, the relative humidity could reach a maximum value of 100% and a minimum value of 33%, which is related to the climatic conditions in the area of the burial chamber location. However, the humidity inside the chamber ranged from 42% to 89% and was highly responsive to seasonal variations, with higher levels in summer and lower levels

in winter. The humidity in winter was reduced both inside and outside the chamber. Considering the above temperature variations, the wind speed imposed a similar effect on the temperature and humidity variations in the burial chamber. In summer, the wind speed was lower, and heat and humidity transfer between inside and outside the burial chamber was reduced. Thus, a higher relative humidity could be maintained inside the burial chamber.

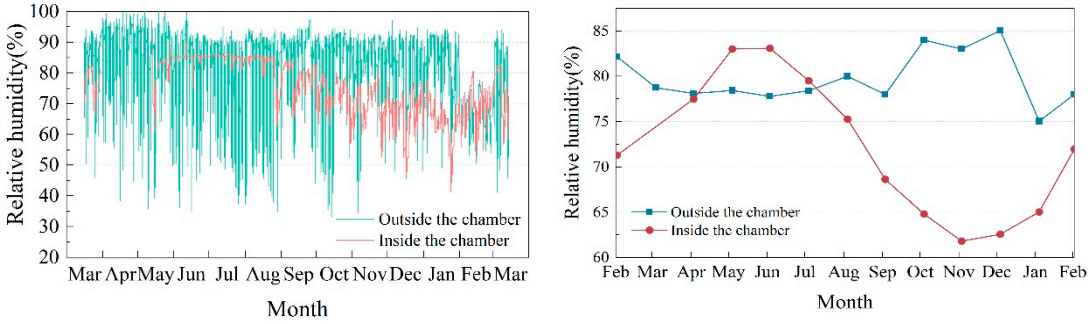

Figure 4. Variations in the relative humidity inside and outside the chamber: (**a**) annual variations; (**b**) average monthly variations.

The average monthly relative humidity inside and outside the chamber (Figure 4b) were analyzed. As shown in the above figure, there was a clear seasonal pattern of the relative humidity variation inside the chamber, reaching a higher level in summer and a lower level in winter, while the average monthly relative humidity outside the chamber remained high throughout the year. The relative humidity outside the chamber was lower than inside the chamber in summer, which is due to the higher temperature outside the chamber. The air water vapor content outside the chamber was higher than that in winter, but the saturated water vapor pressure was more notably affected by the temperature and sharply increased, resulting in a lower relative humidity outside the chamber than inside the chamber.

Combined analysis of Figures 3b and 4b reveals that the temperature inside the burial chamber was lower than that outside the chamber in summer due to water vapor transport to areas with lower temperatures during heat and moisture transfer. Therefore, water vapor was transported into the chamber, and the relative humidity inside the chamber became higher than that outside the chamber. During the other seasons, the temperature inside the chamber was higher than that outside the chamber due to the lower atmospheric temperatures, and water vapor was transported to the outside during heat and humidity transfer, so the relative humidity outside the chamber was higher than that inside the chamber.

3.2. Monthly Variation Patterns of the Temperature and Humidity in the Burial Chamber

3.2.1. Relationship between the Temperature and Radiation Variations in Different Months

Figure 5 shows the relationship between the temperature and radiation variations in Yang Chan's tomb in different months. As shown in the figure, the change in the temperature outside the chamber suitably agreed with the change in the total radiation and fluctuated with total radiation change, while the temperature notably increased. In contrast, there existed no significant correlation between the temperature and total radiation variations inside the chamber, and the overall trend remained stable. Although the temperatures inside and outside the chamber increases, the variations were small. Notably, the temperature inside the chamber is affected by the atmospheric temperature outside the chamber. In the underground system, the effect of the atmospheric temperature is slightly buffered.

Due to the high responsiveness of the solar radiation and the temperatures inside and outside the chamber to seasonal variations, the temperatures inside and outside the chamber were lower in winter due to the low solar radiation and exhibited a decreasing trend. Moreover, they demonstrated an increasing trend in summer due to the higher solar radiation.

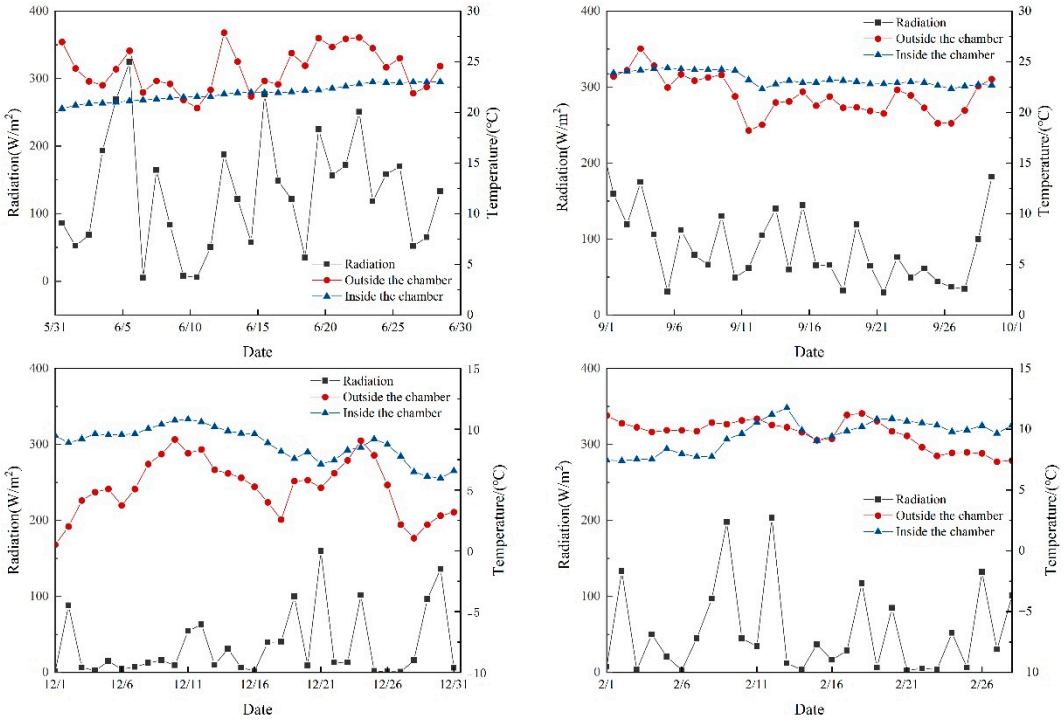

Figure 5. Variations in the temperature of sensor #1 inside the chamber of Yang Can's tomb and the average hourly radiation of the day in the different months.

3.2.2. Variations in the Relative Humidity in Relation to Rainfall in Different Months

As shown in Figure 6, there was a correlation between the relative humidity levels inside and outside the chamber and rainfall variation. The relative humidity outside the chamber was strongly influenced by rainfall, and it peaked at higher rainfall, but the peak exhibited a certain lag. Whereas the relative humidity inside the chamber fluctuated less with rainfall, its peak also exhibited a lag during some seasons. The relative humidity outside the chamber remained high and considerably varied from month to month. The relative humidities inside and outside the chamber were low in winter and spring due to the low rainfall. However, the values fluctuated more notably in winter and spring when the relative humidities inside and outside the chamber were significantly elevated, peaking at high rainfall. Afterward, the relative humidity decreased. In summer and autumn, due to the higher rainfall, the relative humidity inside the chamber fluctuated less and remained consistently high, i.e., rainfall did not significantly affect the value.

3.3. Changes in the Daily Variations in the Temperature and Humidity in the Burial Chamber

3.3.1. Relationship between the Temperature and Radiation Variations throughout the Day

According to Table 2 and Figure 7, the amount of radiation during the day is related to sunrise. During the pre- and post-sunset periods on different days, the radiation is close to zero, and the atmospheric temperature inside the chamber decreases. After sunrise, the amount of solar radiation increases, as does the atmospheric temperature outside the chamber. Notably, the change in the atmospheric temperature outside the chamber is closely related to solar radiation during the different seasons. This suggests that the variations in the atmospheric temperature outside the chamber are directly influenced by solar radiation, and there is consistency in the trends of these variations. The temperature inside the chamber does not greatly change throughout the day (it basically remains constant), with slight fluctuations during the different seasons due to the temperature variations outside the chamber, but all these variations lag behind the temperature variations outside the chamber. The temperature inside the chamber at different depths essentially remains constant in

spring, summer and autumn, slightly higher at shallower depths and fluctuating at the same rate, with slightly higher values at larger depths in the winter months.

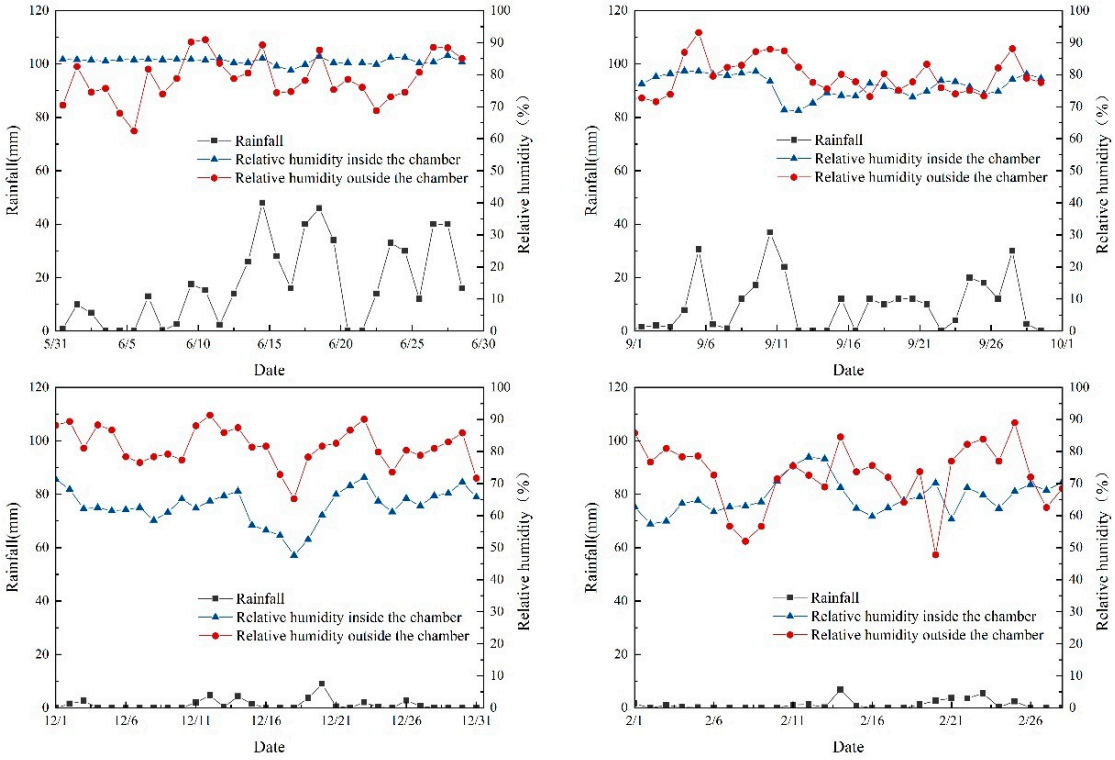

Figure 6. Variations in the relative humidity of sensor #1 inside the chamber of Yang Can's tomb and the average hourly rainfall of the day in the different months.

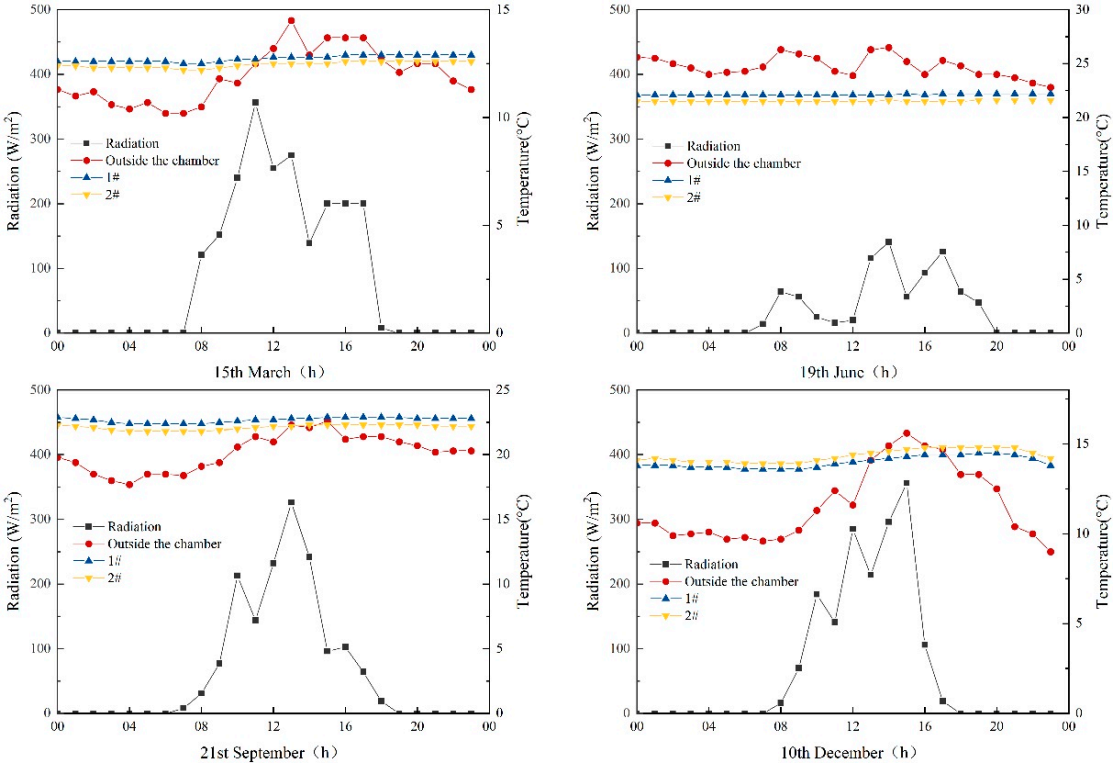

Figure 7. Variations in the temperature of sensor #1 and #2 inside the chamber of Yang Can's tomb and radiation on different days.

Table 2. Sunrise and sunset schedule during the monitoring period in Honghuagang District, Zunyi.

Date	Sunrise	Midnoon	Sunset	Day Length	Daybreak	Dark
3.15	7:01:16	13:01:07	19:00:57	11:59:41	6:38:00	19:24:13
6.19	5:56:46	12:53:43	19:50:40	13:53:54	5:30:11	20:17:15
9.21	6:40:03	12:45:09	18:49:47	12:09:16	6:17:13	19:13:05
12.10	7:31:52	12:44:52	17:57:52	10:26:00	7:06:23	18:23:21

3.3.2. Relative Humidity versus Rainfall throughout the Day on Different Dates

As shown in Figure 8, there were significant fluctuations in the relative humidity outside the chamber after the onset of rainfall. The increase in the relative humidity outside the chamber was greater and increased faster during heavy rainfall. The relative humidity decreased as rainfall tapered off. The relative humidity outside the chamber had already gradually increased before rainfall, which is related to the accumulation of water vapor prior to rainfall. During the period after rainfall, the humidity outside the chamber gradually returned to normal. The variations in the humidity outside the chamber caused by rainfall indicated a certain lag. This suggests that rainfall significantly affected the variations in the relative humidity outside the chamber.

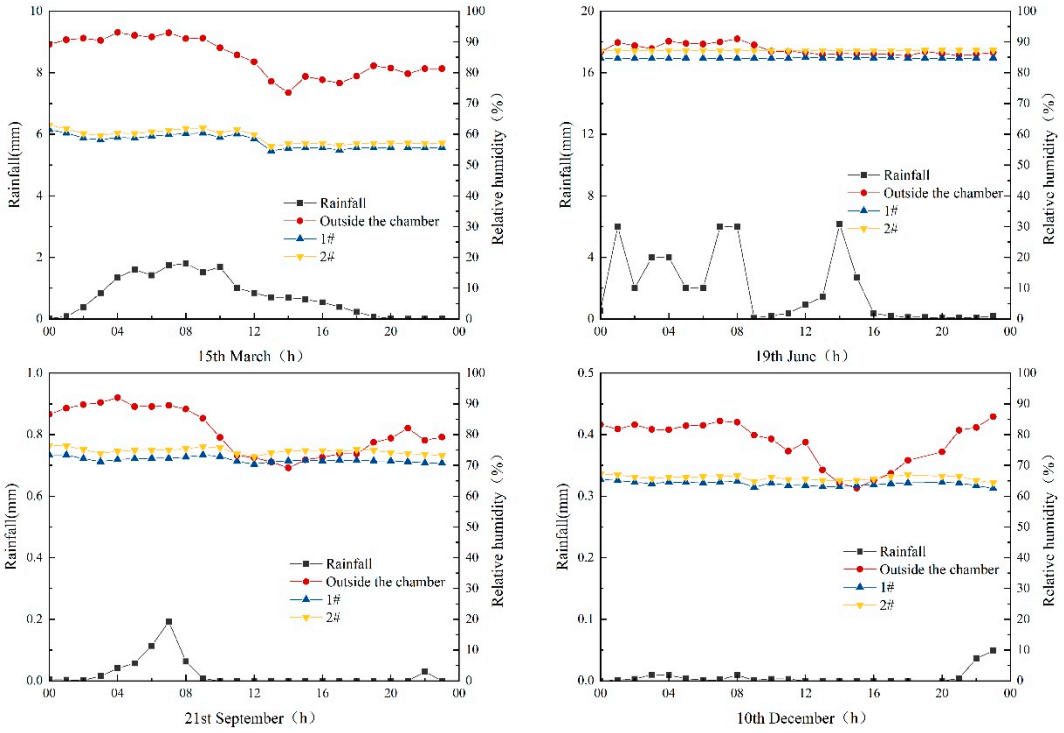

Figure 8. Variations in the humidity of sensor #1 and #2 inside the chamber of Yang Can's tomb and rainfall on different days.

The relative humidity inside the chamber remained relatively constant and low over the course of the day. Even during rainfall periods, the relative humidity inside the chamber increased only slightly and recovered more quickly than that outside the chamber. The humidity trends were consistent across the different depths of the chamber, with a slightly higher relative humidity inside the chamber at greater depths than at shallower depths, regardless of the season.

4. Temperature and Humidity Fitting Model for Stone Burial Relics

4.1. Simulation Software

The simulation software used in this paper is COMSOL Multiphysics 5.6. COMSOL is finite element multi-physics field simulation software that can be used to numerically

simulate and emulate most physical problems encountered in engineering. It provides the advantages of high modeling speed, notable computing power and convenient visualization and analysis. It has been widely used in simulation research in various fields, such as the construction and chemical industries.

4.2. Modeling of Heat and Moisture Transfer in Porous Media

The material used for the construction of the chamber of Yang Can's tomb is sandstone, which is a porous material comprising a solid matrix, wet air, and liquid water, with temperature and moisture transfer features. The presence of dry air, water vapor, and liquid water in the pores of a given porous medium facilitates heat transfer in various ways, such as thermal conductivity, convection, and radiation. Moisture transport can impact the temperature distribution, while moisture transfer accompanied by enthalpy flow and phase change can affect the energy balance in the porous material, which in turn can influence heat transfer. Moisture transfer includes processes such as vapor diffusion, liquid water diffusion, Knudsen diffusion, evaporation and condensation. Heat transfer affects the form in which moisture exists, as well as the moisture transfer coefficient, which in turn affects the moisture distribution in the porous material.

Moisture transfer in porous materials can be divided into three stages, as shown in Figure 9. This paper focuses on the first two stages of moisture migration, as the seepage stage does not normally occur in building structures.

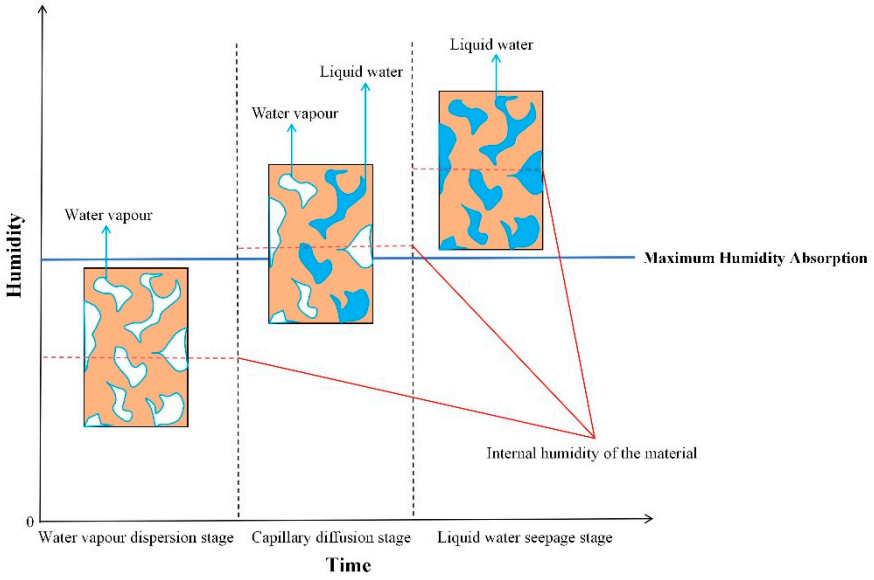

Figure 9. Three stages of moisture transfer in porous materials.

The following assumptions are made to model heat and moisture transfer in the solid materials of Yang Can's tomb:

- The fluids (air, water vapor and liquid water) in the material voids occur in thermal equilibrium;
- The material is a homogeneous, isotropic, continuous medium, with a solid skeleton that does not deform with heat and moisture transfer;
- The effect of the temperature on the equilibrium moisture content in the porous material is neglected;
- Only gas and liquid phases occur in the material pores.

4.2.1. Moisture Transfer

Combined with the law of mass conservation, isothermal hygroscopicity curves, Fick's law, Tetens' model, Darcy's law and Kelvin's relationship, the following moisture transfer equation can be derived:

$$\rho\xi\frac{\partial\varphi}{\partial t}=\frac{\partial}{\partial x}\left[\left(D_vP_{sat}+D_l\rho_lR_v\frac{T}{\varphi}\right)\frac{\partial T}{\partial x}+\left(D_v\varphi\frac{\partial\varphi}{\partial x}+D_l\rho_lR_v\ln(\varphi)\right)\right]\frac{\partial T}{\partial x} \quad (1)$$

where ρ is the density of the material (kg/m^3); ξ is the slope of the isothermal hygroscopic curve of the material; φ is the relative humidity of air (%); D_v is the water vapor diffusion coefficient; P_{sat} is the saturated water vapor partial pressure (Pa); D_l is the liquid water diffusion coefficient; ρ_l is the density of liquid water (kg/m^3); and R_v is the gas constant for water vapor, which is approximately 461 (J/(kg·K)).

4.2.2. Heat Transfer

The following heat transfer equation can be derived from the law of energy conservation and Fourier's law:

$$\rho c_p\frac{\partial T}{\partial t}=\frac{\partial}{\partial x}\left[\left(\lambda+L_vD_v\varphi\frac{\partial P_{sat}}{\partial T}\right)\frac{\partial T}{\partial x}\right]+\frac{\partial}{\partial x}\left(LD_vP_{sat}\frac{\partial\varphi}{\partial}\right) \quad (2)$$

where ρ is the density of the material (kg/m^3); c_p is the specific heat capacity of the material (J/(kg·K)); λ is the coefficient of thermal conductivity (W·m^{-1}·k^{-1}); L_v is the latent heat of vaporization of water vapor (J/kg); and the remaining physical quantities are the same as above.

4.2.3. Boundary Conditions

At the boundary of a given porous medium, where both convection and transfer must be considered, the wet flow rate (g_n) can be expressed as:

$$g_n=\beta\left(\varphi p-\varphi_{surf}p_{surf}\right) \quad (3)$$

where g_n is the wet flow rate (kg/(m^2·s)); β is the surface convective mass transfer coefficient of the porous medium (kg/(Pa·m^2·s)); p is the air saturated water vapor pressure (Pa); φ_{surf} is the relative humidity at the surface of the porous medium (%); p_{surf} is the saturated water vapor pressure at the surface of the porous medium (Pa); and the remaining physical quantities are the same as above.

The heat flux (q_{nt}) can be expressed by the convective heat transfer between the surface of the porous medium and air, latent heat of water vapor and solar radiation:

$$q_{nt}=h\left(T-T_{surf}\right)+L_vg_n+\alpha I \quad (4)$$

where h is the convective heat transfer coefficient at the surface of the porous medium (W/(m^2·K)); T is the temperature of air (K); T_{surf} is the surface temperature of the porous medium (K); α is the solar radiation absorption coefficient; and I is the solar radiation intensity (W/m^2).

4.3. CFD Airflow Modeling

The air inside the chamber can be regarded as a Newtonian fluid whose differential equations must obey the laws of mass, momentum and energy conservation. For turbulent flows, turbulent transport equations must also be considered.

4.3.1. Fluid Flow Control Equations

1. Continuity equation

The mass conservation equation is often referred to as the continuity equation, and the introduction of vector notation $div(a)=\partial a_x/\partial x+\partial a_y/\partial y+\partial a_z/\partial z$, combined with the fact that the density of an incompressible fluid is a constant, yields the following fluid flow continuity equation:

$$div(u)=0 \quad (5)$$

where u is the velocity vector.

2. Momentum conservation equation

For any fluid flow system, the law of momentum conservation must be obeyed. Within the same time interval, the rate of change of the total momentum of each microelement of the flow system is equal to the sum of the various forces acting on this microelement. The equation of momentum conservation is also known as the Navier–Stokes equation (the N–S equation), and combined with the nature of fluid, the following momentum conservation equation for fluid flow can be obtained:

$$\frac{\partial(\rho u)}{\partial t} + div(puu) = div(\mu\ grad\ u) - \frac{\partial p}{\partial x} + F_x \tag{6}$$

$$\frac{\partial(\rho v)}{\partial t} + div(pvu) = div(\mu\ grad\ v) - \frac{\partial p}{\partial y} + F_y \tag{7}$$

$$\frac{\partial(\rho w)}{\partial t} + div(pwu) = div(\mu\ grad\ w) - \frac{\partial p}{\partial z} + F_z \tag{8}$$

where ρ is the fluid density; u, v, and w are the velocity vectors u along the x, y and z directions, respectively; $grad(\ ) = \partial(\ )/\partial x + \partial(\ )/\partial y + \partial(\ )/\partial z$; F_x, F_y, and F_z are the volumetric forces acting on the microelement body along the x, y, and z directions, respectively; p is the pressure acting on the microelement body; and μ is the dynamic viscosity.

3. Energy conservation equation

For any fluid flow system, the law of energy conservation must be obeyed. Within the same time interval, the rate of change of the total energy of each microelement of the flow system is equal to the sum of the heat flux given to the microelement from the outside and the work done by the external force on the microelement, and combined with the nature of fluid, the energy conservation equation can be expressed as follows:

$$\frac{\partial(\rho T)}{\partial t} + div(\rho u T) = div\left(\frac{k}{C_p} grad T\right) + S_T \tag{9}$$

where C_p is the specific heat capacity; k is the heat transfer coefficient of the fluid; and S_T is the viscous dissipation term of the fluid.

In summary, the governing equations for fluid flow can be expressed in the following common form:

$$\frac{\partial(\rho\phi)}{\partial t} + div(\rho u\phi) = div(\Gamma grad\phi) + S \tag{10}$$

where ϕ is the common variable; Γ is the broad diffusion term (generalized diffusion tensor (GDT)); S is the broad source term; and the remaining physical quantities are the same as above. The terms of Equation (10) comprise transient, convective, diffusive, and source terms.

4.3.2. Turbulence Modeling

Turbulence modeling is extremely complex, and it is difficult to fully explain turbulent flow patterns, either by theoretical calculations or experimental studies. Existing turbulence numerical simulation methods can be classified into direct and indirect numerical simulation methods. Non-direct numerical simulation methods mainly include turbulent transport coefficient simulation and large-eddy simulation methods.

The turbulence research object in this paper is the air flow inside the chamber, which belongs to the low-speed turbulent motion category of fluid flow. Turbulence transport coefficient simulation with high accuracy, low computational cost and high reliability was chosen as the solution method in this paper.

1. Time-averaged equation

The turbulent viscosity coefficient μ_T proposed by Boussinesq is introduced, and the following assumptions are made:

$$-\rho\overline{u_i u_j} = \mu_T\left(\frac{\partial \overline{u_i}}{\partial x_j} + \frac{\partial \overline{u_j}}{\partial x_i}\right) \tag{11}$$

The time-averaged momentum transport equation can be obtained as:

$$\frac{\partial}{\partial t}(\rho\overline{u_i}) + \frac{\partial\left(\rho\overline{u_i u_j}\right)}{\partial x_j} = -\frac{\partial \overline{\rho}}{\partial x_i} + \frac{\partial}{\partial x_j}\left[(\mu + \mu_T)\frac{\partial \overline{u_i}}{\partial x_j}\right] + S_i \tag{12}$$

For all variables, the time-averaged transport equation exhibits the following generic form:

$$\frac{\partial\left(\rho\overline{\phi}\right)}{\partial t} + \frac{\partial\left(\rho\overline{u_i}\overline{\phi}\right)}{\partial x_j} = \frac{\partial}{\partial x_j}\left[(\Gamma + \mu_T)\frac{\partial\left(\rho\overline{\phi}\right)}{\partial x_j}\right] + S \tag{13}$$

2. Standard k-ε model

The analysis of the time-averaged equations indicates that the key to calculating turbulent flow is determining μ_T. Many scholars have proposed many solution methods for this purpose. Through the validation study of Xie et al. [23] and Patil M S et al. [24] it can be concluded that the $k-\varepsilon$ model achieves a lower computational cost and higher computational accuracy, so the $k-\varepsilon$ model proposed by Launder [23,24]. The turbulent dissipation rate is denoted in the model and can be defined as follows:

$$\varepsilon = \frac{\mu}{\rho}\overline{\left(\frac{\partial u_i}{\partial x_k}\right)\left(\frac{\partial u_i}{\partial x_k}\right)} \tag{14}$$

The turbulent viscosity coefficient μ_T can be expressed as a function of the turbulent energy k and the turbulent dissipation rate ε.

$$\mu_T = \rho C_\mu \frac{k^2}{\varepsilon} \tag{15}$$

Notably, $C_\mu = 0.99$.

The turbulent kinetic energy k and turbulent kinetic energy dissipation rate ε can be obtained as follows:

$$\frac{\partial}{\partial t}(\rho k) + \frac{\partial}{\partial x_i}(\rho k u_i) = \frac{\partial}{\partial x_i}\left[\left(\mu + \frac{\mu_t}{\sigma_k}\right)\frac{\partial k}{\partial x_j}\right] + G_k - \rho\varepsilon \tag{16}$$

$$\frac{\partial}{\partial t}(\rho\varepsilon) + \frac{\partial}{\partial x_i}(\rho\varepsilon u_i) = \frac{\partial}{\partial x_j}\left[\left(\mu + \frac{\mu_t}{\sigma_\varepsilon}\right)\frac{\partial \varepsilon}{\partial x_f}\right] + C_{1\varepsilon}\frac{\varepsilon}{k}G_k - C_{2\varepsilon}\rho\frac{\varepsilon^2}{k} \tag{17}$$

where G_k is the generating term for the turbulent kinetic energy k due to the mean velocity gradient.

$$G_k = \mu_t S^2 \tag{18}$$

$$S = \sqrt{2S_{ij}S_{ij}} \tag{19}$$

$$S_{ij} = \frac{1}{2}\left(\frac{\partial u_i}{\partial x} + \frac{\partial u_j}{\partial x}\right) \tag{20}$$

Based on experimental validation by Launder et al. and later researchers, the empirical constants of the model take the following values [25]:

$$C_{1\varepsilon} = 1.44,\ C_{2\varepsilon} = 1.92,\ \sigma_k = 1.0,\ and\ \sigma_\varepsilon = 1.3$$

4.4. Physical Modeling

Due to the simulation complexity and computational difficulty, in this study, the inside of the chamber of Yang Can's tomb was moderately simplified with respect to the architectural structure and the connecting steps between the front and back chambers. The inconsistent thicknesses resulting from the stone carvings and the surrounding decorations on the wall surfaces inside the chamber were ignored in the model, and the remainder was modeled according to the actual dimensions. As shown in Figure 10a, the thickness of both the rock wall of the chamber and the concrete waterproof partition wall was set to 0.3 m, the width of the canal between the concrete wall and the main body of the sandstone chamber was set to 0.5 m, and the thickness of the overburden of the upper part of the concrete waterproof partition wall was set to 0.8 m. The left side of the chamber and the upper interface of the soil are in contact with the atmosphere outside the chamber.

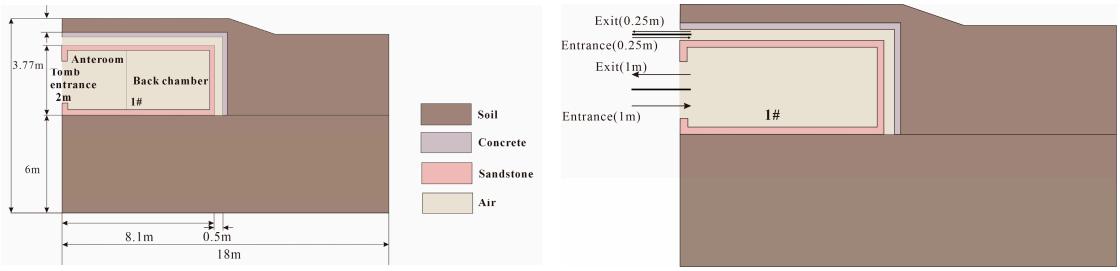

(**a**) (**b**)

Figure 10. Yang Can's tomb model: (**a**) physical model; (**b**) entrance and exit settings.

4.4.1. Material Parameters

In this paper, sandstone and concrete were treated as enclosures in the simulations and as building materials in COMSOL. The hygrothermal physical parameters of sandstone are listed in Table 1, those of concrete and soil were retrieved from the literature [26,27].

4.4.2. Boundary Conditions

In this paper, a nonstationary heat and moisture coupling simulation process was used, and one year of temperature and humidity monitoring data outside the chamber was used as boundary conditions at the interface between the soil and outdoor air at the top of the chamber, and the convective heat transfer coefficient was set to 18 W/(m^2·K).

A heterogeneous air distribution was considered inside the chamber under the influence of airflow, which is correlated with the air temperature, humidity and velocity during hygrothermal migration in the walls. As shown in Figure 10b, both the space inside the chamber of Yang Can's tomb and the canal between the chamber and the concrete waterproof partition wall are single-channel spaces. The upper part of the door of the chamber is defined as the exit, and the lower part is defined as the entrance in model construction, with the dimensions of both the entrance and exit reaching 1 m. The canal between the chamber and the concrete waterproof partition wall was similarly established, with the dimensions of both the entrance and the exit reaching 0.25 m.

At the entrance to the chamber, data on the meteorological parameters outside the chamber, including atmospheric temperature, relative humidity and wind speed, were used to determine the flow rate, air temperature and relative humidity, considering that external air currents could enter the interior of the chamber.

4.4.3. Initial Conditions

As shown in Figure 11, the initial conditions of the model include a soil temperature of 15 °C and a relative humidity of 80%. The settings for the remaining section include a temperature of 12.8 °C and a relative humidity of 87.5%.

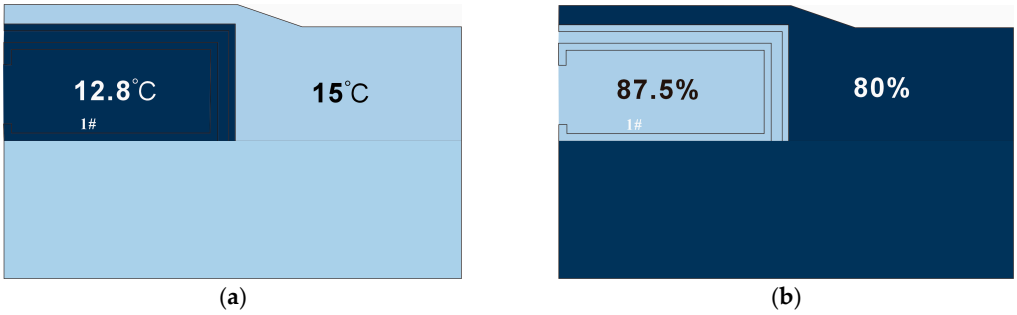

Figure 11. Initial conditions of Yang Can's tomb model: (**a**) temperature conditions; (**b**) relative humidity conditions.

4.4.4. Mesh Subdivision

The mesh subdivision of Yang Can's tomb model is shown in Figure 12. The inside chamber, canal, boundary and corner parts are carefully divided.

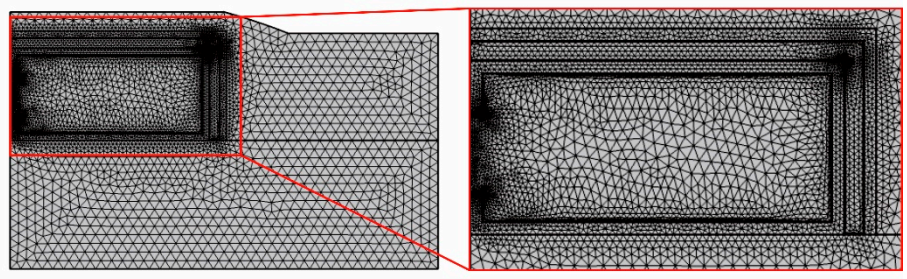

Figure 12. Yang Can's tomb model meshing and local enlargement.

4.5. Validation of the Simulation Results

To verify the simulation accuracy considering the complex chamber environment, the model calculation results were compared to the measured data. Due to the similarity of the monitoring data across the different depths, only the results for measurement point #1 were selected for comparison. A comparison of the simulation results of the air temperature and relative humidity inside the chamber with the measured data is shown in Figure 13.

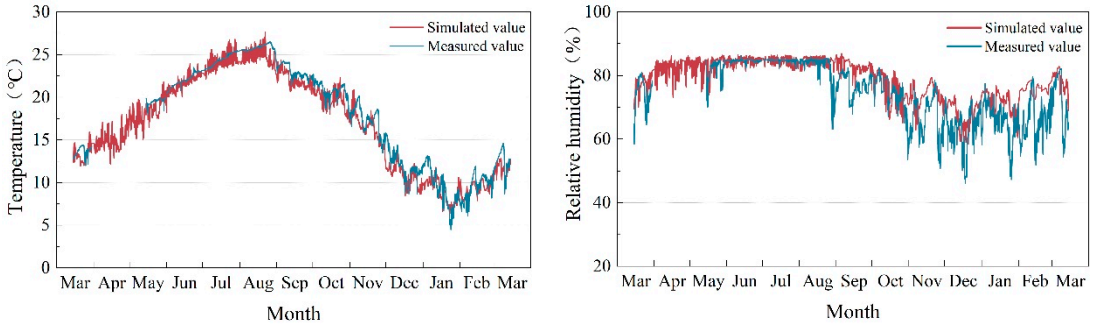

Figure 13. Comparison of the simulated and measured air temperatures and relative humidities inside the chamber.

In the temperature simulations, the difference between the maximum measured and simulated values is 1.539 °C, while the difference between the minimum measured and

simulated values is 0.195 °C. Moreover, there is a certain lag in the peak values of the measured values relative to the simulated values. In the humidity simulations, the difference between the measured and simulated values is 0.174% for the maximum values and 1.628% for the minimum values. In contrast to the temperature simulations, the measured peak values occur slightly ahead of the simulated values.

Figure 13 reveals that the simulation results approximately conform with the measured values, and the trends of the simulated air temperature and humidity variations are basically consistent with those of the measured data. The simulation results are more accurate in the summer months (the simulation results highly agree with the measured values). Moreover, the modeled values fit the measured values better at higher relative humidity levels and slightly worse at lower relative humidity levels in winter, but the difference is not significant. The above reflects the suitable predictive ability of the model for complex environments.

4.6. Model Evaluation and Extension

The error analysis results indicate that:

(1) Theoretical modeling errors occur, which cannot be avoided. Notably, scholars often establish theoretical models based on certain basic assumptions, such as fluid and solid mechanics in the assumption of a continuous medium. Many theoretical models have been proposed based on specific physical conditions, such as the turbulence model in CFD analysis, while some model parameters are obtained through specific experiments, yielding empirical parameters. Therefore, a reasonable choice of theoretical models is critical. In this study, a heat and moisture transfer model and CFD model are combined to provide better simulations of the physical problem studied and to avoid error sources that could lead to large errors.

(2) For any engineering problem, numerical simulation requires geometric modeling of the computational domain based on the actual physical conditions. Since the actual conditions are often very complex, some simplifications of the physical geometry are needed in the calculation process, so a certain error will be generated. Some geometric simplifications, however, do not affect the results and can be ignored. In this study, certain simplifications of the geometric modeling setup are made, but the resulting errors can be neglected relative to the full model.

(3) The mesh quality, accuracy, and type all contribute to the discretization error. This phenomenon is caused by the mesh division. Moreover, to ensure the mesh accuracy, if the mesh size is infinitesimally small, more systems of algebraic equations must be solved, but the solutions obtained will be more accurate. In this paper, more refined meshing is employed for certain locations, which reduces the error.

(4) Boundary conditions enable equations to provide deterministic solutions and various input parameters for solving a particular physical problem. This is usually determined by the actual physical conditions. However, some parameters must be obtained experimentally. In this study, a few experimental measurements are conducted and averaged to determine the parameters and boundary conditions that contribute to minimizing the experimental errors.

The difference between the simulated and measured values mainly stems from the fact that the actual environment is affected by numerous factors, while the model has been moderately simplified. Hence, the error between the simulated results and measured data is reasonable. Such differences reflect the complexity of the real environment and provide valuable lessons for model improvement and optimization.

The above comparison results demonstrate that the proposed heat and humidity transfer–CFD airflow model achieves high accuracy and reliability in simulating the inside chamber environment of Yang Can's tomb. Therefore, in the process of research and protection of stone cultural relics in other tomb categories, computer simulations can be performed and combined with relevant information and external environmental conditions to explore the internal environment, which can reduce the damage and destruction of cultural relics caused by monitoring.

5. Conclusions

In this study, the following conclusions can be obtained by monitoring the inside and outside of the chamber of Yang Can's tomb for a period of one year, combined with indoor tests and simulations:

1. The characteristics of the temperature and humidity variations of stone relics in tombs are closely related to the direct solar radiation and rainfall. The temperature variations outside the chamber are mainly influenced by solar radiation, while the relative humidity is notably influenced by rainfall. The temperature and humidity inside the chamber are mainly affected by variations in the temperature and humidity outside the chamber. The wind speed indirectly affects the temperature and humidity inside the chamber by influencing the hygrothermal transfer effect. The temperature and humidity variations inside the chamber exhibit a lag due to the buffering effect of the envelope on the temperature and humidity variations outside the chamber. The greater the chamber depth is, the poorer the air circulation with the outside and the higher the relative humidity.
2. The temperature and humidity variations in Yang Can's tomb exhibit seasonal variation characteristics. The temperature outside the chamber reaches a maximum value of 37.8 °C in summer and a minimum value of −1.4 °C in winter. The temperature inside the chamber is less responsive to seasonal variations, and the seasonal variation magnitude is small. The humidity outside the chamber remains high throughout the year and does not significantly vary with the season. The humidity inside the chamber is more responsive to seasonal variations, with a higher humidity in summer and a lower humidity in winter.
3. A heat and humidity transfer—CFD airflow model is established to simulate the inside chamber environment of Yang Can's tomb. Through comparison and validation against the measured data, the model achieves favorable applicability and high reliability. Temperature and humidity data for the outside environment of the chamber can be used to predict the temperature and humidity inside the chamber. This study provides a reference and basis for subsequent research and protection of stone cultural relics in the tomb category.
4. By studying the change trends of the temperature and humidity inside and outside the tomb, it can be found that the temperature and humidity inside the tomb are mainly affected by those outside the tomb. The higher the humidity is, the greater the damage to stone cultural relics. Therefore, structures or plants can be arranged at the entrance of the tomb with stone cultural relics to alleviate the overall impact of the atmospheric temperature and humidity on the temperature and humidity within the chamber. Moreover, chamber desiccant or dehumidifier technology can be used to reduce the humidity in the chamber.

Author Contributions: Conceptualization, P.L. and B.S..; methodology, W.S. and X.X.; validation, W.S.; formal analysis, W.S., X.X. and Q.W.; investigation, C.L.; writing—original draft preparation, W.S. and X.X.; writing—review and editing, P.L. and B.S.; funding acquisition, P.L. and B.S. All authors have read and agreed to the published version of the manuscript.

Funding: This work was supported by the National Natural Science Foundation of China (No. 51408285 and No. 42267023), the Natural Science Foundation of Gansu Province (No. 20JR5RA293), the Fundamental Research Funds for the Central Universities (No. lzujbky-2021-57), the Science and Technology Item Foundation of Northwest Research Institute Limited Company of CREC, the Education Science and Technology Innovation Project of Gansu Province and the Education Reform Research Project of Lanzhou University.

Institutional Review Board Statement: Not applicable.

Informed Consent Statement: Not applicable.

Data Availability Statement: The authors confirm that the data supporting the findings of this study are available within the article.

Acknowledgments: We thank our colleagues at Northwest Research Institute Limited Company of China Railway Engineering Corporation for their great help in this work. We thank the editors for their patience processing our manuscript. The anonymous reviewers are gratefully acknowledged for their careful and insightful reviews.

Conflicts of Interest: Author Bo Sun was employed by the company Heritage Protection Science and Innovation Center, Northwest Research Institute Co. Ltd. of C.R.E.C. The remaining authors declare that the research was conducted in the absence of any commercial or financial relationships that could be construed as a potential conflict of interest.

References

1. Liu, X. New Understanding of Tombs in Ancient China: A Case Study of Han Period Tombs. *Archaeol. Cult. Relics* **2020**, *4*, 64–69.
2. Matsukura, Y.; Oguchi, C.T.; Kuchitsu, N. Salt Damage to Brick Kiln Walls in Japan: Spatial and Seasonal Variation of Efflorescence and Moisture Content. *Bull. Eng. Geol. Environ.* **2004**, *63*, 167–176. [CrossRef]
3. Van Belleghem, M.; Steeman, M.; Janssen, H.; Janssens, A.; De Paepe, M. Validation of a Coupled Heat, Vapour and Liquid Moisture Transport Model for Porous Materials Implemented in CFD. *Build. Environ.* **2014**, *81*, 340–353. [CrossRef]
4. Gu, Z.; Luo, X.; Meng, X.; Wang, Z.; Ma, T.; Yu, C.; Rong, B.; Li, K.; Li, W.; Tan, Y. Primitive environment control for preservation of pit relics in archeology museums of China. *Environ. Sci. Technol.* **2013**, *47*, 1504–1509. [CrossRef] [PubMed]
5. Luo, X.; Gu, Z.; Wang, Z.; Tian, W.; Li, K. An independent and simultaneous operational mode of air conditioning systems for visitors and relics in archaeology museum. *Appl. Therm. Eng.* **2016**, *100*, 911–924. [CrossRef]
6. Song, P.; Luo, X.; Tian Wei, T.; Gu, Z. Numerical simulation of environmental control for relics preservation in the funerary pit by air curtain system. *Procedia Eng.* **2017**, *205*, 265–272. [CrossRef]
7. An, C. A preliminary study on the application of non-stationary heat and humidity coupling simulation technology in China's stone cultural relics. *Cult. Relics* **2016**, *04*, 91–96.
8. Araoka, W.; Hokoi, S.; Ogura, D. Deterioration and Preservation of City Wall in Nanjing. Nordic Symposium on Building Physics. *Energy Procedia* **2017**, *132*, 945–950. [CrossRef]
9. Chang, B.; Luo, X.; Shen, Y.; Li, J.; Gu, Z. Experimental Investigation on an Evaporative Cooling System for the Environmental Control in Archaeology Museum. In Proceedings of the 11th International Symposium on Heating, Ventilation and Air Conditioning, Harbin, China, 13 July 2019; Wang, Z., Zhu, Y., Wang, F., Wang, P., Shen, C., Liu, J., Eds.; Springer: Singapore, 2020; pp. 201–209.
10. Sadłowska-Sałęga, A.; Radoń, J. Feasibility and Limitation of Calculative Determination of Hygrothermal Conditions in Historical Buildings: Case Study of St. Martin Church in Wiśniowa. *Build. Environ.* **2020**, *186*, 107361. [CrossRef]
11. Luo, X.; Dang, Y.; Yu, C.W.; Gu, Z. The Practice of Local Environment Control for the Funerary Pits of Emperor Qin's Mausoleum Site Museum. *Indoor Built Environ.* **2021**, *30*, 293–297. [CrossRef]
12. Frasca, F.; Verticchio, E.; Cornaro, C.; Siani, A.M. Performance Assessment of Hygrothermal Modelling for Diagnostics and Conservation in an Italian Historical Church. *Build. Environ.* **2021**, *193*, 107672. [CrossRef]
13. Bi, W.; Yan, Z.; Zhang, Z.; Yao, S.; Zhang, J.; Wang, X. Modeling and Numerical Simulation of Heat and Mass Transfer in the Cave Wall of the Mogao Grottoes in China. *Build. Environ.* **2021**, *201*, 108003. [CrossRef]
14. Xiong, J.; Li, A.; Liu, C.; Dong, J.; Yang, B.; Cao, J.; Ren, T. Probing the Historic Thermal and Humid Environment in a 2000-Year-Old Ancient Underground Tomb and Enlightenment for Cultural Heritage Protection and Preventive Conservation. *Energy Build.* **2021**, *251*, 111388. [CrossRef]
15. Mouneer, T.; Aly, M.; Mina, E. Experimental Investigation and CFD Modelling for Indoor Air Thermal Conditions in Worship Buildings in Egypt: Church and Masjid. *Eng. Res. J.* **2022**, *175*, 341–398. [CrossRef]
16. Xu, Y.; Zeng, Z.; Sun, D. Experimental and Numerical Investigation on the Effect of Heat and Moisture Coupling Migration of Unsaturated Lateritic Clay for the Soil Thermal Storage System. *Energy Build.* **2022**, *276*, 112499. [CrossRef]
17. Liu, Z.; Zhang, Y.; Peng, H. Energy Balanced Routing Protocol Based on Improved Particle Swarm Optimisation and Ant Colony Algorithm for Museum Environmental Monitoring of Cultural Relics. *IET Smart Cities* **2023**, *5*, 210–219. [CrossRef]
18. Cao, J.; Li, T. Analysis of Spatiotemporal Changes in Cultural Heritage Protected Cities and Their Influencing Factors: Evidence from China. *Ecol. Indic.* **2023**, *151*, 110327. [CrossRef]
19. Xia, C.; Liu, D.; Kong, Z.; Xie, H.; Mu, B.; Hokoi, S.; Li, Y. Spatial and Temporal Changes in Microclimate Affect Disease Distribution in Two Ancient Tombs of Southern Tang Dynasty. *Heliyon* **2023**, *9*, e18054. [CrossRef]
20. Liu, F.; Zhang, X.; Zeng, J.; Li, Y.; Wang, G. The Numerical Study on Indoor Heat and Moisture Transfer Characteristics of an Ancient Palace Building in Beijing. *Processes* **2023**, *11*, 1900. [CrossRef]
21. Shi, J. Yang Can's Tomb in Zunyi. *Contemp. Guizhou* **2007**, *79*, 52.
22. *ISO 15148:2002(en)*; Hygrothermal Performance of Building Materials and Products—Determination of Water Absorption Coefficient by Partial Immersion. ISO: Geneva, Switzerland, 2002. Available online: https://www.iso.org/obp/ui/#iso:std:iso:15148:ed-1:v1:en (accessed on 29 June 2023).
23. Xie, H.; Zhang, S.; Guan, X. Effects of Turbulence Model and Wall Functions on the Numerical Simulation of Indoor Air Flow. *J. Univ. Shanghai Sci. Technol.* **2017**, *39*, 5.

24. Patil, M.S.; Cho, C.-P.; Lee, M.-Y. Numerical Study on Thermal Performances of 2.0 kW Burner for the Cabin Heater of an Electric Passenger Vehicle. *Appl. Therm. Eng.* **2018**, *138*, 819–831. [CrossRef]
25. Launder, B.E.; Spalding, D.B. *Lectures in Mathematical Model of Turbulence*; Academic Press: Cambridge, MA, USA, 1972.
26. Tariku, F.; Kumaran, K.; Fazio, P. Transient Model for Coupled Heat, Air and Moisture Transfer through Multilayered Porous Media. *Int. J. Heat Mass Transf.* **2010**, *53*, 3035–3044. [CrossRef]
27. Li, K.; Zhang, X.; Han, X.; Zhu, D.M. Experimental Research of Water Vapor Permeability through Building Materials. *J. Build. Mater.* **2009**, *12*, 288–291.

Disclaimer/Publisher's Note: The statements, opinions and data contained in all publications are solely those of the individual author(s) and contributor(s) and not of MDPI and/or the editor(s). MDPI and/or the editor(s) disclaim responsibility for any injury to people or property resulting from any ideas, methods, instructions or products referred to in the content.